Design Method for Reducing AC Resistance of Traction Motor Using High Fill Factor Coil to Improve the Fuel Economy of eBus

Kyoung-Soo Cha, Jun-Woo Chin, Soo-Hwan Park, Young-Hoon Jung, Eui-Chun Lee, and Myung-Seop Lim, *Member, IEEE*

***Abstract*—To improve electric vehicle (EV) mileage, motors must be designed for higher power density and efficiency. Winding technology with a high fill factor decreases the motor volume by reducing the unnecessary area of the slot. A motor conductor with a large cross-sectional area generates additional losses due to ac resistance, reducing the efficiency of the motor. Traction motors designed under these conditions can adversely affect EV fuel economy. Therefore, a design method is proposed to reduce the ac resistance of a traction motor by applying winding technology with a high fill factor to increase the fuel economy of the EVs. First, the characteristics and manufacturing process of the maximum slot occupation (MSO) coil, which is a winding technology with a high fill factor, are introduced. An ac resistance reduction method for a motor using an MSO coil is then proposed. Additionally, a motor designed using the proposed method is presented, and its electrical performance is compared with that of an initial motor. Next, the effect of the fuel economy improvement of the presently designed traction motor is verified through a vehicle simulation, and the validity of this article is experimentally confirmed using this motor.**

***Index Terms*—AC resistance, electric vehicle, fuel economy, high fill factor, maximum slot occupation (MSO) coil, power density, traction motor, vehicle simulation.**

I. Introduction

RECENTLY, many studies on electric vehicles (EVs) have been conducted owing to environmental pollution regulations [1]. Moreover, some cities have restricted the movement of non-emission-free vehicles [2]. However, despite these regulations, an obstacle to increased EV use is its low energy density and long battery charging time. Therefore, research is required to increase the mileage and fuel economy of EVs. The latest studies to increase the fuel efficiency of EVs have been concerned with energy management strategies and components [3], [4]. Among the studies on improving the fuel economy of EVs, those on traction motors are typically focused on high power density and efficiency [5], [6].

Studies on the high power density of traction motors have been approached from two perspectives: increasing output power with constant volume and reducing volume with constant power. Dhulipati *et al.* [7], [8] utilized a multiphase motor and [9] installed a field coil and permanent magnet in the rotor of a wound field synchronous motor. In addition, Fatemi *et al.* [10] investigated the optimal design of a motor, increasing the power density by reducing its volume.

In addition to the aforementioned methods, applying a winding technology with a high-fill-factor to the motor is effective in improving the power density. A commonly used conventional round wire winding for EV traction motors has a fill factor of up to 35–45%; this implies that the cross-sectional area of the dead space between the conductor and the core in the slot is 65–55% of the slot cross-sectional area [11], [12]. As dead space does not contribute to the motor power, reducing the cross-sectional area of the dead space by increasing the fill factor can help to improve power density [11]. In this regard, various winding technologies have been proposed to increase the fill factor: rectangular, hairpin, I-pin, compressed, and Roebel-bar windings [13]–[15]. Park and Lim [16] used a hairpin winding to improve the power density, achieving a fill factor as high as 60%.

The maximum slot occupation (MSO) coil was also invented to increase the fill factor, similar to the aforementioned winding schemes proposed by researchers. The MSO coil was fabricated based on the shape of the slot in the designed motor and can thus have a fill factor of up to 80%. Therefore, the MSO coil with a high fill factor can significantly improve the power density.

However, because winding technologies with high fill factors, including MSO coils, have a large conductor cross-sectional area, the resistance increases dramatically at high frequencies owing to skin and proximity effects, which are commonly expressed as ac resistance. The ac resistance caused by operation at high frequencies adversely affects the motor efficiency in

Manuscript received September 22, 2020; revised December 11, 2020; accepted January 11, 2021. Date of publication January 26, 2021; date of current version June 15, 2021. Recommended by Technical Editor X. Hu and Senior Editor V. Ivanov. This research was supported by the Korea Institute of Industrial Technology (KITECH). *(Corresponding author: Myung-Seop Lim.)*

Kyoung-Soo Cha, Jun-Woo Chin, Soo-Hwan Park, and Myung-Seop Lim are with the Department of Automotive Engineering, Hanyang University, Seoul 04763, South Korea (e-mail: chakungsoo@hanyang.ac.kr; cjw1254@hanyang.ac.kr; shwanp14@hanyang.ac.kr; myungseop@hanyang.ac.kr).

Young-Hoon Jung is with the R&D Division, Hyundai Motor Company, Hwaseong 18280, South Korea (e-mail: yh.jung@hyundai.com).

Eui-Chun Lee is with the Korea Institute of Industrial Technology, Daegu 42990, South Korea (e-mail: 2chun@kitech.re.kr).

Color versions of one or more figures in this article are available at https://doi.org/10.1109/TMECH.2021.3054798.

Digital Object Identifier 10.1109/TMECH.2021.3054798

the high-speed region. Thus, using a high-fill-factor winding helps us to improve the power density, but makes it difficult to achieve high efficiency in the high-speed region. Therefore, it is necessary to reduce the ac resistance when applying a winding technology with a high fill factor to EV traction motors, as the goal is to achieve high motor efficiency.

Generally, in the industry, strands are transposed along the slot to reduce ac resistance. Petrov *et al.* [17] reported a comparison of ac resistance with and without the use of strands. Paradkar and Böcker [18], [19] reported a reduction in ac resistance due to winding transposition. However, a reduction in the ac resistance of MSO coils is unachievable using these methods because MSO coils are structurally incapable of using strands.

Recently, research on MSO coils is being actively conducted. Chin *et al.* [20] investigated the effect of current density and the number of parallel circuits on the ac resistance of MSO coils. Park *et al.* [21] reported the occurrence of no-load losses in an MSO coil. Lee *et al.* [22] reported the thermal and electrical characteristics of a motor with an MSO coil. However, no studies have proposed a design method for reducing the ac resistance of MSO coils or confirmed the effect of the ac resistance design method on the system.

The purpose of this article is to improve fuel economy by improving the efficiency of the traction motor, which is a component of an electric bus (eBus). The method to increase the fuel economy of a vehicle can be described in two steps. First, an ac resistance reduction design method for a motor applying winding technology with a high fill factor is proposed. Second, the effect on the fuel efficiency of the vehicle using a motor designed with the proposed method is confirmed through a vehicle simulation.

This article presents a method of improving fuel economy by reducing the ac resistance of EV traction motors using MSO coils. First, the features of the MSO coil and the manufacturing process of the motor with the MSO coil are introduced. Second, a stator design method for reducing the ac resistance of the motor with MSO coils is proposed. The proposed method changes the slot width by changing the tooth width under the condition of a constant slot and conductor cross-sectional area. The slot width is a significant design variable for reducing the ac resistance, as it affects the magnetic leakage flux in the slot, which in turn affects the ac resistance. Here, an initial and improved motor are presented and compared. The improved motor is redesigned using the proposed method to reduce the ac resistance. Furthermore, a vehicle simulation was performed for the same driving cycle and EV, based on the efficiency map of each motor, to compare the fuel economy according to the motor. Finally, an improved motor was fabricated and tested to validate this article.

II. MSO Coil

The MSO coil^{TM} was developed by the Korea Institute of Industrial Technology (KITECH) [20]–[23]. Fig. 1 presents the structure and an application example of the MSO coil. The MSO coil can achieve a fill factor of up to 80%. The fill factor of conventional round wire winding can extend up to 40%; thus, the fill factor of the MSO coil is twice that of the round wire winding.

Fig. 1. Structure and application example of MSO Coil.

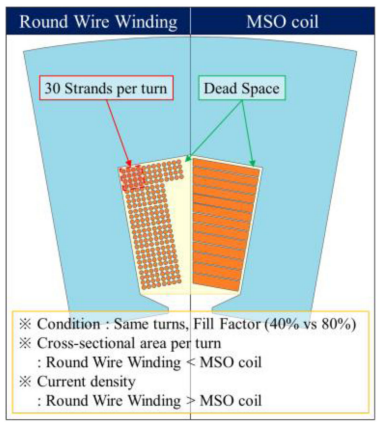

Fig. 2. Dead space between conductor and core in slot according to winding technology.

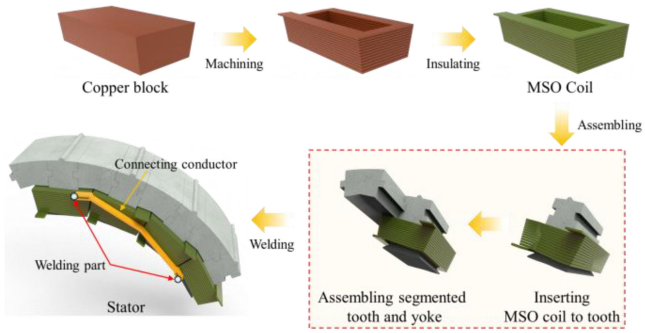

Fig. 3. Manufacturing process of motor with MSO coil.

As shown in Fig. 2, compared to the round wire winding, the MSO coil can reduce the dead space between the conductor and core in the slot.

The manufacturing process of a motor with an MSO coil is depicted in Fig. 3. The process can be divided into four steps: machining, insulating, assembling, and welding [23]. In the machining step, a copper block is machined considering the shape of the slot and the number of turns. Because the shape of the slot is taken into account when fabricating the MSO coil, it can achieve a higher fill factor than the other winding technologies. In the insulating step, the MSO coil is insulated using Teflon and polyimide to prevent short-circuits between the turns. In the assembling step, the MSO coil is assembled with a stator. The stator core is manufactured by dividing it into yoke and tooth parts for assembly with the MSO coil. Finally, in the

welding step, the MSO coil and end coil are welded to make the connection between the MSO coils of the same phase.

The MSO coil has several advantages and disadvantages. The advantages of the MSO coils are as follows:

1) As the fill factor of the MSO coil is up to 80%, various motor design methods can be proposed. If the cross-sectional area of the conductor is increased, the dc resistance and current density can be reduced, thereby improving the efficiency and thermal performance. Alternatively, if the cross-sectional area of the conductor is maintained and the cross-sectional area of the dead space is reduced, the stator size can be reduced, thereby improving the power density and torque density.
2) MSO coils have better heat dissipation performance than other winding technologies, owing to the large contact area between the conductor and core. The power of the motor can be improved by applying a large current density, owing to the good heat dissipation performance of MSO coils compared to other winding technologies. Alternatively, the motor cooling system can be simplified by applying the same current density.

The disadvantages of MSO coils are as follows:

1) The armature winding method is limited to tooth concentrated winding, as MSO coils are machined from a copper block. Therefore, the number of pole–slot combinations is limited.
2) The ac resistance of the conductor becomes extremely high owing to the skin effect and proximity effect at high speeds; this is due to the large cross-sectional area of the conductor. As a result, the high ac resistance causes the efficiency to decrease at high speeds.

Owing to the advantages and disadvantages of MSO coils mentioned above, MSO coils can be said to be suitable for motors with the following characteristics: high power density, low speed, high torque. These motor types are used for traction motors for hybrid electric vehicles and commercial vehicles, in-wheel motors, etc. However, even if MSO coils are applied to these applications, the issue of ac resistance at high speeds must be resolved. In the industry, strands are used or are transposed along the slot to reduce ac resistance. These methods cannot be used owing to the structural limitations of MSO coils. Therefore, it is necessary to study a method of ac resistance reduction that is applicable to the MSO coil.

III. AC Resistance Reduction Design of Motor Using MSO Coil

This section presents the ac resistance reduction design method and design results using the proposed method. First, the major design factor for reducing the ac resistance of a motor using MSO coils is presented through an analysis of the ac resistance equation in the slot. The ac resistance reduction design is performed based on the tendency of the motor output and ac resistance according to the change in the major design factor, and design results such as copper loss, iron loss, and efficiency are compared and analyzed.

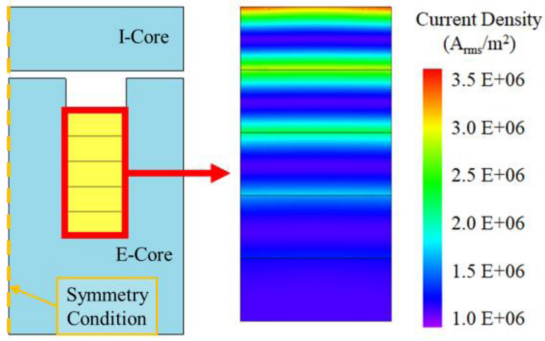

Fig. 4. Current density distribution in conductor within EI core.

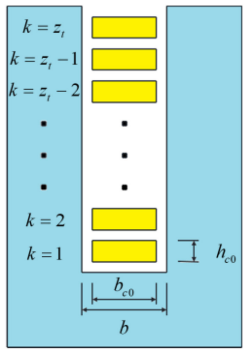

Fig. 5. Reference model to analytically calculate the current density distribution within slot.

A. Basic Principle of AC Resistance

Under the high-frequency condition, the current density distribution in the conductor is nonuniform. For example, Fig. 4 shows the current density distribution in a rectangular conductor within E- and I-shaped cores. The figure indicates that the current density distribution is not uniform and is concentrated at a specific location. An uneven current density distribution causes additional losses in conductors. In addition, a larger conductor cross-sectional area results in a greater current density concentration in a specific location, which causes additional losses due to ac resistance.

Fig. 5 shows a reference model for the analytical calculation of ac resistance within the slot. The equation of the ac resistance factor for the analytical calculation is referenced from [24]. The ac resistance factor is calculated based on the dimensions of the conductor and the slot.

To verify the equation of the ac resistance factor, the calculation results were compared to the results of a 2-D finite element analysis (FEA). The nonlinearity of the core was ignored. In addition, the tendency of the ac resistance factor with respect to the shape change of the slot was examined to confirm whether the tendency depends on the slot shape. In this case, the fill factor and cross-sectional area of the slot were the same, but the slot shape changed. Therefore, the shape of the slot changes according to the tooth width. If the tooth width increases, the yoke and slot become narrower. Conversely, if the tooth width

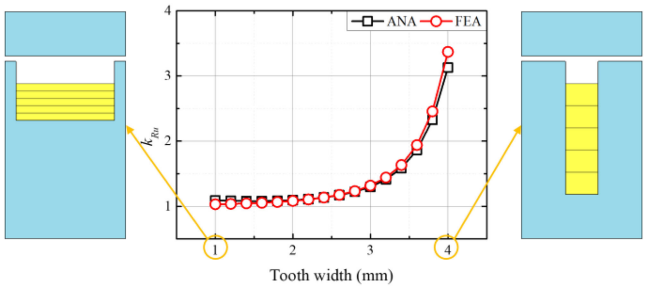

Fig. 6. Example of the analytical model and results.

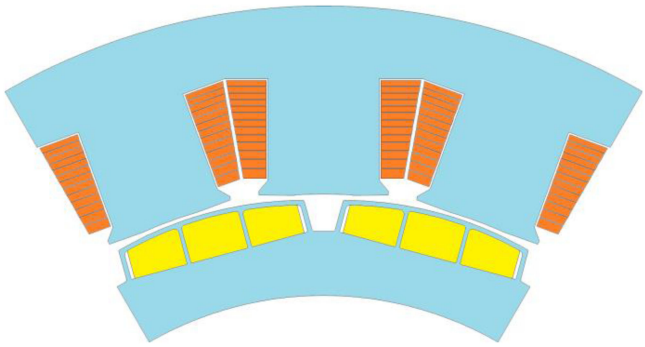

Fig. 7. Shape of initial motor.

TABLE I
SPECIFICATION REQUIRED FOR ELECTRIC BUS

Items	Unit	Value
Maximum Torque	Nm	800
Maximum Power	kW	130
Base Speed	RPM	1600
Maximum Speed	RPM	5200
DC Voltage	V_{DC}	360
Maximum Line Current	A_{rms}	500
Stator Outer Diameter	mm	210
Stack Length	mm	83

TABLE II
EXPERIMENTAL POINTS FOR MULTI-OBJECTIVE OPTIMIZATION

No.	Tooth Width (mm)	Yoke Width (mm)
1	14.00	35.92
2	17.00	34.75
3	20.00	33.42
4	23.00	31.90
5	26.00	30.10
6	29.00	28.11
7	32.00	25.66
8	35.00	22.93
9	38.00	19.51
10	41.00	15.49
11	44.00	10.68

decreases, the yoke and slot become wider; and the shape of the conductor is almost the same as that of the slot, which is also a feature of the MSO coil, as shown in Fig. 2. The electromagnetic field was analyzed using the JMAG software package, which is currently used by many companies and research institutes.

Fig. 6 shows the comparison between the calculated ac resistance factor using the equation and 2-D FEA. As shown in Fig. 6, the tendency of the ac resistance factor calculated using the analytical method is similar to that calculated using 2-D FEA. In addition, the narrower the tooth width, the smaller the ac resistance factor; that is, the ac resistance factor increases as the widths of the slot and conductor become narrower. This is because the slot leakage flux decreases as the slot width increases, reducing the skin and proximity effects on the conductor within the slot. Therefore, it can be inferred that the tooth width in the stator is a major factor in designing a motor using an MSO coil.

B. Stator Design Considering AC Resistance

Fig. 7 depicts the shape of the initial motor, and Table I lists the specification requirements for the eBus traction. The maximum torque and power required for the eBus traction are 800 N·m and 130 kW, respectively. For the operation of the traction motor, the nominal voltage of the battery and the maximum line current magnitude are 360 V_{DC} and 500 A_{rms}, respectively, and the current density of the traction motor is 11 A_{rms}/mm^2.

As mentioned in Section III-A, when designing a motor that uses a conductor with a large cross-sectional area and operates at high frequencies, the additional loss due to ac resistance must be considered. Motors with a narrow tooth width have a small ac resistance factor, which can reduce additional losses caused by ac resistance, thereby contributing to the high efficiency of the motor in the high-speed region. However, a narrow tooth width may not achieve the maximum torque required by the vehicle system at the base speed owing to the saturation of the core. Therefore, the motor should be designed considering the maximum torque required by the vehicle system at the base speed and the ac resistance at high speed.

A multi-objective optimization with the kriging surrogate model was conducted using in-house codes to find the optimal design point under multiple operating conditions [25], [26]. The optimization objectives can be defined as

$$\min : \begin{cases} f_1(x) = W_{c\_base} \\ f_2(x) = W_{c\_max} \end{cases} \tag{1}$$

where f_i is the objective function, x is the design parameter, W_{c_base} is the copper loss at the base speed, and W_{c_max} is the copper loss at the maximum speed.

In addition to the optimization objectives, considering that the torque may be reduced owing to machine loss or manufacturing tolerances, the constraints were determined as 105% of the required torque of the vehicle system. The constraints can be expressed as follows:

$$\begin{cases} g_1(x) = 800 \times 1.05 - T_{\text{base}} \le 0 \\ g_2(x) = 238.9 \times 1.05 - T_{\max} \le 0 \end{cases} \tag{2}$$

where g_i is the constraint, T_{base} is the maximum torque required by the vehicle system at the base speed, and $T_{\max}$ is the maximum torque required by the vehicle system at the maximum speed.

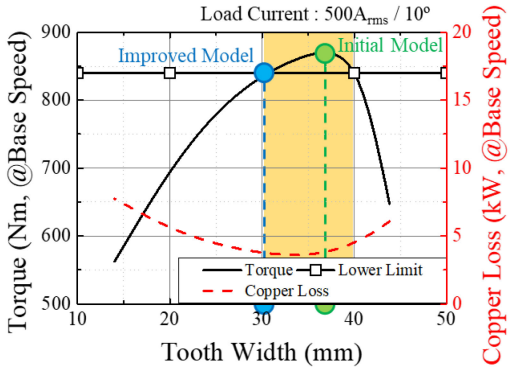

Fig. 8. Torque and copper loss according to tooth width at base speed.

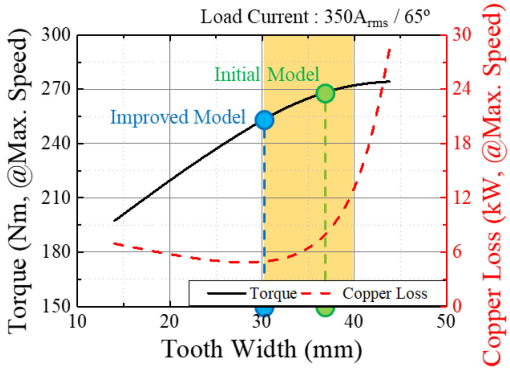

Fig. 9. Torque and copper loss according to tooth width at maximum speed.

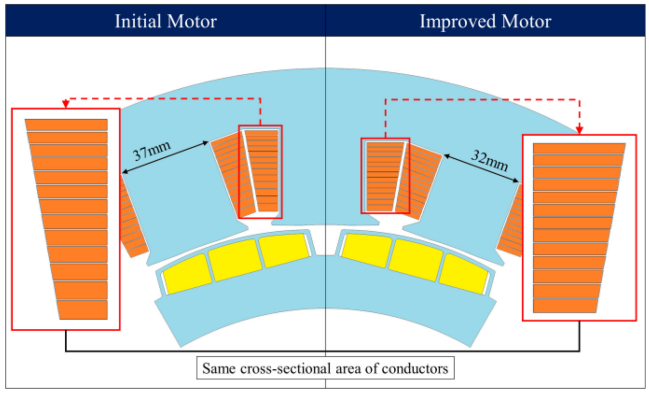

Fig. 10. Shape of initial and improved motors.

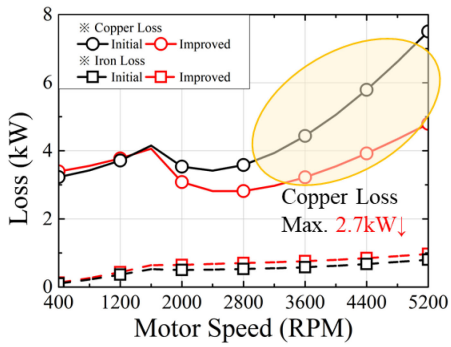

Fig. 11. Copper loss and iron loss of the characteristic curve according to motors.

Table II lists the experimental points for the multi-objective optimization. The tooth width is a design variable, and the upper and lower boundaries are 14 and 44 mm, respectively. As the tooth width changes uniformly, the yoke width is determined by the geometric relationship with the tooth width under the same slot cross-sectional area. The applied current in each condition is given by the current that generates the maximum torque of the initial motor, according to the motor speed.

Fig. 8 shows the torque and copper loss according to the tooth width at the base speed, and Fig. 9 shows those at the maximum speed. The orange-shaded regions in Figs. 8 and 9 indicate the tooth width range that satisfies the constraints. As shown in Fig. 8, the copper loss is similar within this range, indicating that the ac resistance is almost similar within this range. Conversely, within the range indicated in orange in Fig. 9, the maximum copper loss is approximately three times the minimum copper loss. Only the resistance affects the copper loss as the current remains the same in this analysis. As a result, the tooth width affects the ac resistance at the maximum speed.

An improved motor was designed through multi-objective optimization. Fig. 10 depicts the shape of the initial and improved motors. As shown in Fig. 10, the tooth widths of the initial and improved motors are 37 and 32 mm, respectively, and the slot width of the improved motor is wider than that of the initial motor. As a result, when the same current is applied at the maximum speed, the copper loss of the improved motor is reduced by approximately 34% compared to that of the initial motor.

C. Comparison of Motor Electrical Characteristics

In this section, the electrical characteristics of the initial and improved motors are compared. The effect of the proposed design method on the characteristics of the motor using the MSO coil was simulated and verified by analyzing the efficiency as well as the characteristic curves with respect to torque, speed, and current of the improved motor via nonlinear 2-D FEA.

All potential losses, such as copper, iron, and mechanical losses, were considered to derive accurate simulation results. To calculate the copper loss, the resistance of the coil was separately calculated by dividing the coil into two parts: the coil side and end [27]. For the iron loss, the test result of the core material used in manufacturing the motor was used in the FEA [28]. In addition, the mechanical losses of the motor were considered through a no-load test of the manufactured motor [29].

Fig. 11 shows the copper loss and iron loss of the characteristic curve when the initial and improved motors are controlled using the maximum torque per ampere (MTPA) algorithm [30]. In Fig. 11, the straight lines with circle symbols indicate copper losses, and the dashed lines with square symbols indicate iron losses. As shown in Fig. 11, the copper loss is considerably larger than the iron loss, and it can be expected to significantly affect

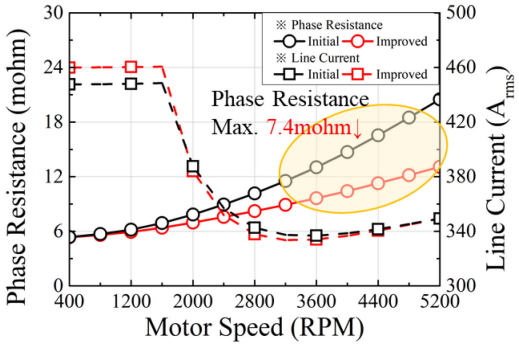

Fig. 12. Phase resistance and current magnitude of the characteristic curve according to motors.

the motor efficiency. In addition, the copper loss of the improved motor increased compared to that of the initial motor at speeds of less than ∼1600 r/min, and the iron loss of the improved motor increased compared to that of the initial motor across the entire speed range. Therefore, the electrical loss of the improved motor increased in the low-speed region. However, the decrease in the copper loss in the high-speed region was larger than the increase in the iron loss. In particular, the iron loss of the improved motor increased by 0.2 kW, but the copper loss decreased by 2.7 kW, and the total electrical loss decreased by 2.5 kW at 5200 r/min.

The copper loss was investigated in detail to analyze why the electrical loss improvement effect of the improved motor was different in the low- and high-speed regions. The copper loss is related to the phase resistance and current magnitude. Therefore, the phase resistance and current magnitude of the characteristic curve were investigated. Fig. 12 shows the phase resistance and current magnitude of the characteristic curve when the initial and improved motors are controlled using the MTPA algorithm. In the figure, the phase resistance is indicated by a straight line with circle symbols, and the line current magnitude is represented by a dashed line with square symbols. At low speeds, the phase resistances of the initial and improved motors are almost the same; however, the phase resistance of the initial motor increases sharply as the speed increases owing to the skin and proximity effects. As a result, the phase resistance of the improved motor is up to 7.4 mΩ smaller than that of the initial motor. On the contrary, the tendency of the current magnitude is different from that of the phase resistance. As shown in Fig. 8, because the reluctance of the improved motor is large, the current required for the improved motor to generate the same output power at low speed is 12 A_{rms} more than that for the initial motor. For these reasons, the copper loss of the improved motor is larger at low speeds and smaller at high speeds than that of the initial motor.

Fig. 13 shows efficiency maps of the initial and improved motors calculated via FEA. As shown in Figs. 13(a) and (b), the efficiency of the two motors is similar at low speeds; however, the efficiency of the improved motor at high speeds is remarkably superior to that of the initial motor. Fig. 13(c) shows a map of the difference in efficiency between the two motors, allowing a direct comparison. As shown in Fig. 13(c), at speeds less than 2800 r/min, the efficiency of the improved motor increases or decreases compared to that of the initial motor but remains similar. However, at speeds higher than 2800 r/min, the efficiency of the improved motor increases remarkably as the speed increases by up to 4.01%p. Thus, it was confirmed that the efficiency was improved by reducing the ac resistance at high speeds while maintaining almost the same efficiency at low speeds owing to the proposed design method. In the next section, a vehicle simulation based on the analysis results in this section is presented to compare the fuel economy.

IV. Vehicle Simulation

This section presents the vehicle simulations conducted to calculate the fuel economy when a target vehicle has completed a given driving cycle. In addition, the effect of ac resistance reduction design on fuel economy improvement according to the bus type is analyzed through the simulation. The simulation was performed using the advanced vehicle simulator (ADVISOR), developed by the National Renewable Energy Laboratory [31]–[33]. Fig. 14 shows a schematic of the vehicle simulation. Vehicle simulations require the specifications of the target vehicle, efficiency maps of the traction motor, and specifications regarding the battery and selected driving cycle. In this section, the vehicle simulation is described in detail, and the results of a simulation performed to compare the fuel economy according to the motor are presented.

A. Theoretical Basis of Vehicle Simulation

The vehicle simulation is performed based on the dynamic equation of the vehicle. Resistive and traction forces affect the motion of the vehicle. Fig. 15 presents the dynamic force diagram of a vehicle. There are three resistive forces: rolling resistance, aerodynamic drag, and grade resistance. These are calculated using data from the driving cycle and vehicle model.

The total resistive force can be expressed as

$$\begin{aligned} F_{Total} &= F_R + F_G + F_D \\ &= f_R M_v g \cos\theta + M_v g \sin\theta + \tfrac{1}{2}\rho A_F C_D (V_v + V_W)^2 \end{aligned} \tag{3}$$

where F_{Total} is the total resistive force, F_R is the rolling resistive force, F_G is the grading resistive force, F_D is the aerodynamic drag force, f_R is the rolling resistance coefficient, M_v is the vehicle mass, g is gravitational acceleration, θ is the longitudinal slope angle, ρ is the air density, A_F is the frontal area, C_D is the aerodynamic drag coefficient, V_v is the vehicle speed, and V_w is the wind speed.

The traction force is calculated using the total resistive force and the required vehicle acceleration. The vehicle acceleration is determined by the target driving cycle. The traction force is

$$F_T = F_{Total} + M_V a \tag{4}$$

where F_T is the traction force and a is the required vehicle acceleration.

The required torque of the motor is

$$T_M = \frac{r_w F_T}{n_G \eta_G} \tag{5}$$

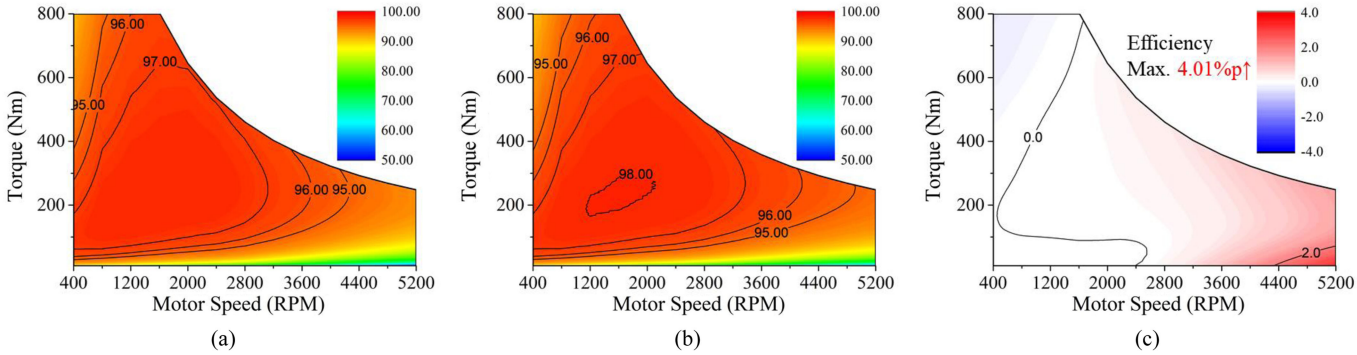

Fig. 13. Efficiency map: (a) initial motor, (b) improved motor, and (c) difference between initial and improved motors.

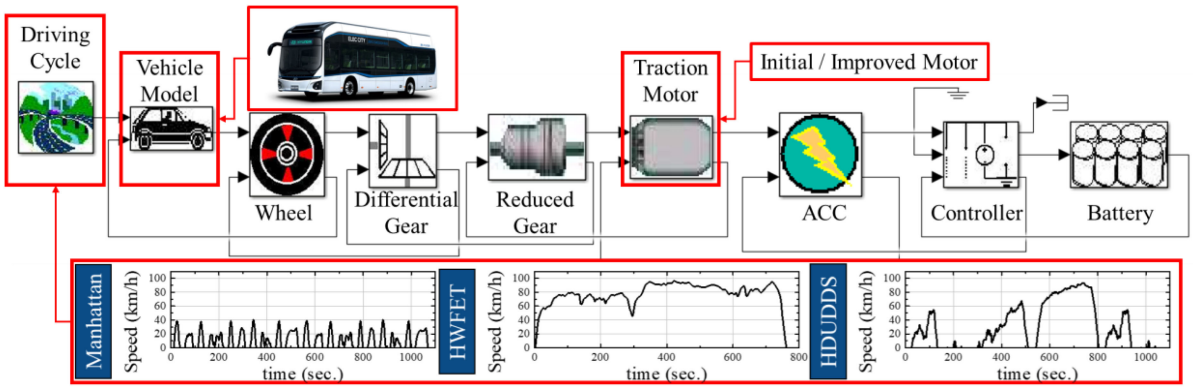

Fig. 14. Schematic of vehicle simulation.

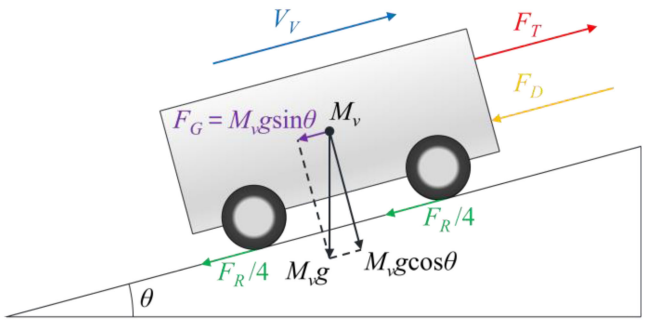

Fig. 15. Dynamic force diagram of vehicle.

where T_M is the required torque of the motor, r_w is the wheel radius, n_G is the gear ratio, and η_G is the gear efficiency.

The required speed of the motor in rpm is given by

$$N_M = \frac{60}{2\pi r_W} n_G V_V. \tag{6}$$

B. Vehicle Simulation Condition

The target vehicle was an eBus. Table III lists the specifications of the target vehicle, and Table IV lists the drive conditions. The efficiency of the gear and inverter is assumed to be 95%.

TABLE III
SPECIFICATION OF TARGET VEHICLE

Items		Unit	Value
Curb Weight		kg	12500
Frontal Area		m^2	6.72
Overall Width		m	2.50
Overall Height		m	3.21
Overall Length		m	10.58
Wheelbase		m	5.95
Wheel Radius		m	0.48
Inverter	Efficiency	%	95
Gear	Ratio	-	9.5
	Efficiency	%	95
Battery	Overall Nominal Voltage	V_{DC}	360
	Overall Nominal Capacity	kWh	256

TABLE IV
DRIVE CONDITION

Items	Unit	Value
Air Density	kg/m^3	1.28
Gravitational Acceleration	m/s^2	9.81
Aerodynamic Drag Coefficient	-	0.7
Rolling Resistance Coefficient	-	0.007
Number of Passengers	-	40
Weight per Passenger	kg	65

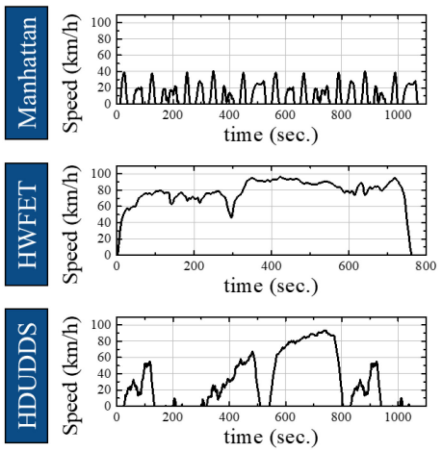

Fig. 16. Target driving cycle.

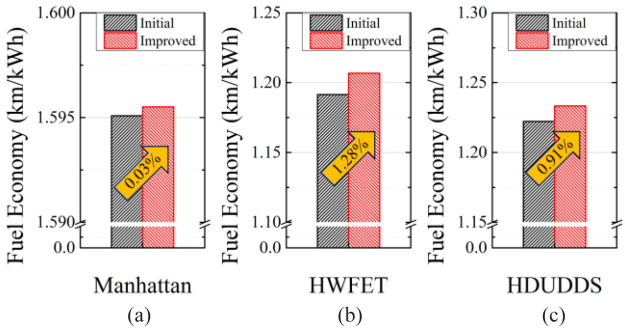

Fig. 17. Fuel economy according to motors. (a) Manhattan. (b) HWFET. (c) HDUDDS.

The efficiency map of the traction motor was obtained based on the FEA, as shown in Figs. 13(a) and (b).

Fig. 16 shows the target driving cycle used for the vehicle simulation. There are three driving cycles: the Manhattan bus cycle (Manhattan), highway fuel economy driving schedule (HWFET), and heavy-duty urban dynamometer driving schedule (HDUDDS). The Manhattan cycle was developed based on actual observed driving patterns of transit buses in the Manhattan district of New York City, and the HWFET cycle is a chassis dynamometer driving schedule developed by the US EPA for determining the fuel economy of vehicles on the highway. The HDUDDS cycle was developed for testing chassis dynamometers for heavy-duty vehicles. As shown in Fig. 16, the HDUDDS cycle seems to have both the characteristics of the low-speed operation of the Manhattan cycle and the high-speed operation of the HWFET cycle. Therefore, each driving cycle for the EV was chosen to consider typical driving patterns of different bus types. The bus types are as follows:

1) transit bus: drives between short stops in the downtown area;
2) express bus: drives long distances between cities;
3) suburban bus: drives medium-length distances within the metropolitan area.

C. Results of Vehicle Simulation

Vehicle simulations were performed to verify the effectiveness of the proposed design method under the same conditions; the results were analyzed to confirm whether the proposed method increases the fuel economy as only the motor characteristics differ in the vehicle simulations.

Fig. 17 presents the fuel economy of the vehicle using each motor. In the Manhattan cycle, the fuel economy of the vehicle using the improved motor slightly increased compared to that of the vehicle using the initial motor but it was almost the same. However, in the HWFET cycle, the fuel economy of the vehicle using the improved motor improved by 1.28%, from 1.19 to 1.21 km/kWh. In addition, the fuel economy of the vehicle using the improved motor in the HDUDDS cycle increased by 0.91% from 1.22 to 1.23 km/kWh.

Fig. 18 shows the motor operating proportion map of the motor for each driving cycle. The motor operating proportion map is effective for analyzing the motor operating points. The heat map in the middle of the map represents the motor operating proportion. The darker the color on the heat map, the more often the motor is operating. In addition, the bar graphs at the top and right of the motor proportion map show the motor operating proportion according to the speed and torque. Therefore, through the motor proportion map, the features for the distribution of operating points under different driving cycles are compared. First, the main operating point of the motor is confirmed through a heat map. In the Manhattan cycle, the speed of the main operating point is 1000 r/min, but in the HWFET and HDUDDS cycles, the speed of the main operating point is 4600 r/min. Next, the motor operating proportion according to the speed is concentrated in the high-speed and low-speed regions in the HWFET and Manhattan cycles, respectively. On the contrary, in the HDUDDS cycle, the operating points are evenly distributed over the entire speed region. Finally, the motor operating proportions of motoring and regenerative braking were analyzed. In the HWFET and HDUDDS cycles, the motor performs more motoring operations than regenerative braking operations. However, in the Manhattan cycle, the motor performs more regenerative braking operations compared to the other cycles. For this reason, the fuel economy of the vehicle is higher in the Manhattan cycle than in the other cycles, as shown in Fig. 17.

Fig. 19 presents a map denoting the influence of the operation points on the fuel economy. The operation points in the Manhattan cycle are evenly distributed in the areas where the efficiency of the improved motor is good and poor. For this reason, there is little difference between the fuel economy of vehicles according to the motors in the Manhattan cycle. Unlike the Manhattan cycle, the operation points of the motor in the HWFET cycle are concentrated in the high-speed region. The improved motor has excellent efficiency improvement effects in the high-speed region, and thus vehicles using the improved motor demonstrate a remarkable improvement in fuel economy compared to vehicles using the initial motor. In addition, even in the HDUDDS cycle, the high-speed operation of the motor contributed to improving the fuel economy of vehicles using the improved motor. Therefore, the two motors exhibit almost the

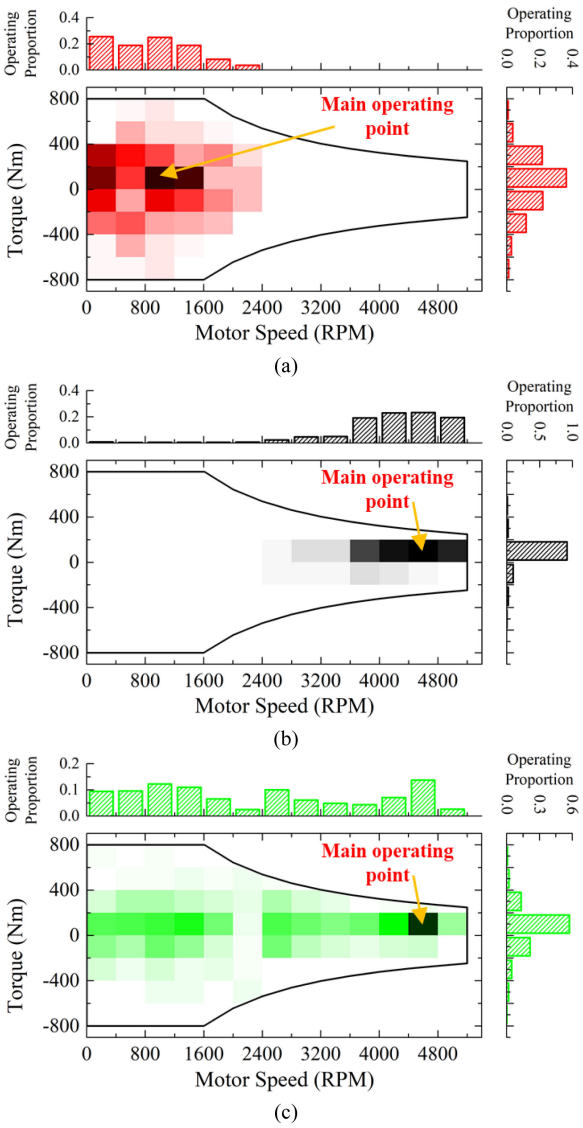

Fig. 18. Motor operating proportion map according to driving cycles. (a) Manhattan. (b) HWFET. (c) HDUDDS.

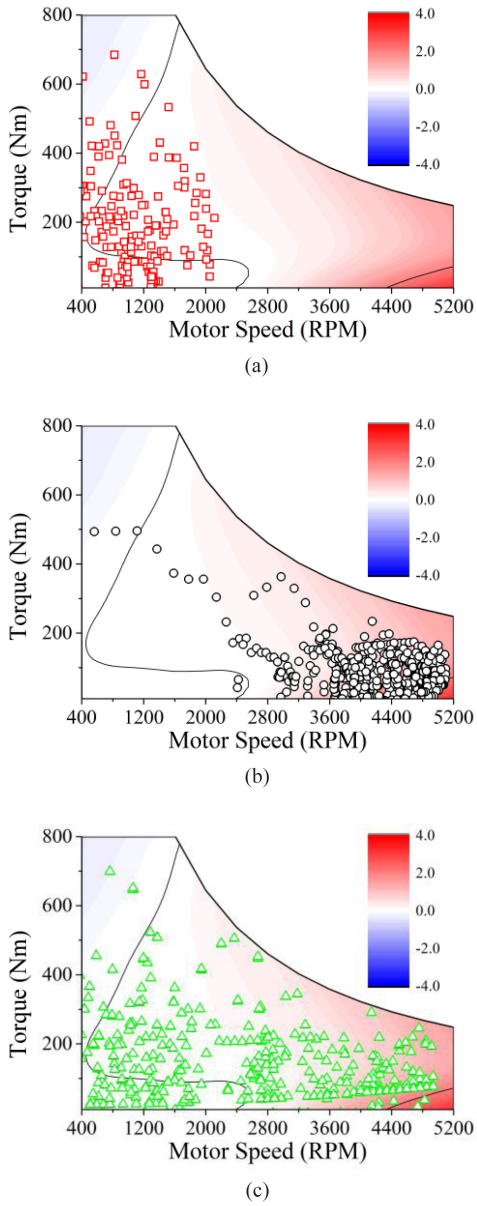

Fig. 19. Motor operation point on efficiency difference map. (a) Manhattan. (b) HWFET. (c) HDUDDS.

same performance when used in a vehicle that stops frequently, such as a transit bus; however, for a vehicle running at high speed, such as an express or suburban bus, the fuel economy of the improved motor is better.

V. Experimental Verification

The validity of the proposed method was experimentally verified using a motor with an MSO coil. Fig. 20 shows the configuration of the experiment and the fabricated sample of the motor with the MSO coil. The equipment for the experiment consisted of inverters, dynamometers, power sources, power analyzers, and torque and speed sensors. The motor was driven with the load conditions obtained from the simulation results through FEA. The input power of the motor was calculated using a power analyzer, and the output power of the motor was calculated using the data measured by the torque and speed sensors. The input and output powers were used to estimate the

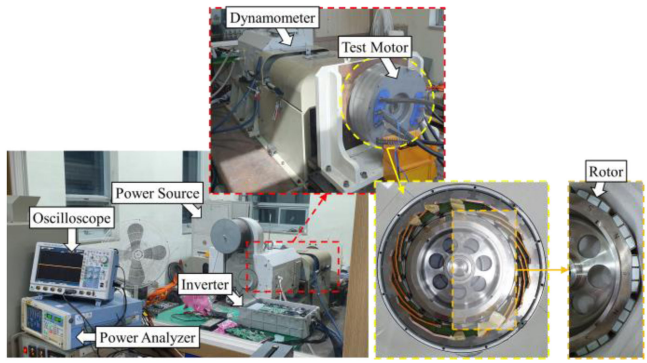

Fig. 20. Configuration of experiment and fabricated sample motor.

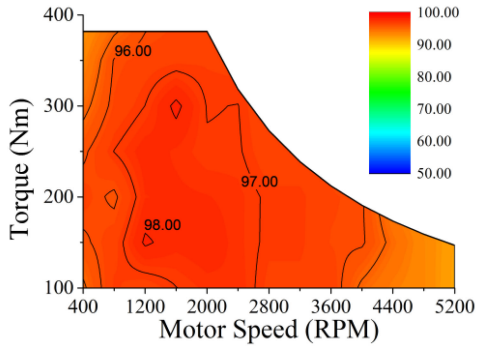

Fig. 21. Efficiency map measured through experiment.

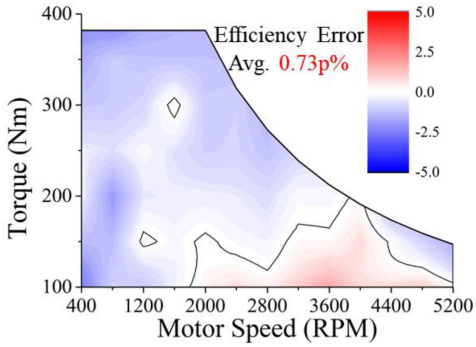

Fig. 22. Efficiency error between 2-D FEA and experiment.

efficiency of the motor. In this experiment, the power and torque were only measured up to approximately 50% of the maximum power and torque owing to the limitations of the dynamometer and sensor.

VI. Conclusion

In this article, a motor design method using MSO coils was proposed to improve the fuel economy of EVs. The MSO coil with a high fill factor can help improve the power density. However, the large cross-sectional area of the MSO coil can reduce efficiency in high-speed regions owing to the skin and proximity effects. For this reason, a design method for a motor with an MSO coil was proposed to satisfy the output and reduce the ac resistance.

The motor improved using the proposed method demonstrated almost the same efficiency as the initial motor in the low-speed region. However, the efficiency of the improved motor was better than that of the initial motor in the high-speed region by up to 4.01%p. Based on this result, a vehicle simulation was performed to calculate the fuel economy of the vehicle according to the motor. When the improved motor was used as the traction motor, the fuel economy remained unchanged in the Manhattan cycle but improved by 1.28% and 0.91% in the HWFET and HDUDDS cycles, respectively. Finally, the validity of the proposed method was confirmed through an experiment using a sample motor fabricated with the MSO coil. The measured efficiency of the motor was almost the same as the simulation results; therefore, the simulation results were considered reliable. It can be concluded that the proposed design method is effective for improving the fuel economy of an EV powered using a motor with an MSO coil.

References

[1] W. Tu *et al.*, "Acceptability, energy consumption, and costs of electric vehicle for ride-hailing drivers in Beijing," *Appl. Energy*, vol. 250, pp. 147–160, 2019.

[2] L. Garfield, "13 cities that are starting to ban cars," *Bus. Insider*, Jun. 2018. [Online]. Available: https://www.businessinsider.com/cities-going-car-free-ban-2017-8

[3] X. Tang, T. Jia, X. Hu, Y. Huang, Z. Deng, and H. Pu, "Naturalistic data-driven predictive energy management for plug-in hybrid electric vehicles," *IEEE Trans. Transp. Electrific.*, early access, Sep. 21, 2020, doi: 10.1109/TTE.2020.3025352.

[4] T. Liu, X. Tang, H. Wang, H. Yu, and X. Hu, "Adaptive hierarchical energy management design for a plug-in hybrid electric vehicle," *IEEE Trans. Veh. Technol.*, vol. 68, no. 12, pp. 11513–11522, Dec. 2019.

[5] D. Kim, K. Cha, M. Lim, and J. Hong, "Rare-Earth-Free electric motor design for EV traction comparing overall vehicle efficiency considering driving cycle," in *Proc. IEEE 84th Veh. Technol. Conf.*, 2016, pp. 1–5.

[6] M. Park, D. Kim, Y. Jung, M. Lim, and J. Hong, "Modeling, design and control of wound-field synchronous motor for high energy efficiency of electric vehicle," in *Proc. IEEE Energy Convers. Congr. Expo.*, 2019, pp. 3960–3967.

[7] H. Dhulipati, E. Ghosh, S. Mukundan, P. Korta, J. Tjong, and N. C. Kar, "Advanced design optimization technique for torque profile improvement in six-phase PMSM using supervised machine learning for direct-drive eV," *IEEE Trans. Energy Convers.*, vol. 34, no. 4, pp. 2041–2051, Dec. 2019.

[8] S. S. R. Bonthu, S. Choi, and J. Baek, "Design optimization with multiphysics analysis on external rotor permanent magnet-assisted synchronous reluctance motors," *IEEE Trans. Energy Convers.*, vol. 33, no. 1, pp. 290–298, Mar. 2018.

[9] S. Hwang, J. Sim, J. Hong, and J. Lee, "Torque improvement of wound field synchronous motor for electric vehicle by PM-assist," *IEEE Trans. Ind. Appl.*, vol. 54, no. 4, pp. 3252–3259, Jul./Aug. 2018.

[10] A. Fatemi, D. M. Ionel, M. Popescu, Y. Chong, and N. A. O. Demerdash, "Design optimization of a high torque density spoke-type PM motor for a formula race drive cycle," *IEEE Trans. Ind. Appl.*, vol. 54, no. 5, pp. 4343–4354, Sep/.Oct. 2018.

[11] M. Popescu, J. Goss, D. A. Staton, D. Hawkins, Y. Chong, and A. Boglietti, "Electrical vehicles—Practical solutions for power traction motor systems," *IEEE Trans. Ind. Appl.*, vol. 54, no. 3, pp. 2751–2762, May/Jun. 2018.

[12] M. C. Kulan, N. J. Baker, and J. D. Widmer, "Design of a high fill factor permanent magnet integrated starter generator with compressed stator windings," in *Proc. 22nd Int. Conf. Elect. Mach.*, 2016, pp. 1–7.

[13] J. D. Widmer, C. M. Spargo, G. J. Atkinson, and B. C. Mecrow, "Solar plane propulsion motors with precompressed aluminum stator windings," *IEEE Trans. Energy Convers.*, vol. 29, no. 3, pp. 681–688, Sep. 2014.

[14] D. Jung, Y. Kim, U. Lee, and H. Lee, "Optimum design of the electric vehicle traction motor using the hairpin winding," in *Proc. IEEE 75th Veh. Technol. Conf.*, 2012, pp. 5–8.

[15] Y. Zhao, D. Li, T. Pei, and R. Qu, "Overview of the rectangular wire windings AC electrical machine," *CES Trans. Elect. Mach. Syst.*, vol. 3, no. 2, pp. 160–169, 2019.

[16] H. Park and M. Lim, "Design of high power density and high efficiency wound-field synchronous motor for electric vehicle traction," *IEEE Access*, vol. 7, pp. 46677–46685, 2019.

[17] I. Petrov, M. Polikarpova, P. Ponomarev, P. Lindh, and J. Pyrhonen, "Investigation of additional AC losses in tooth-coil winding PMSM with high electrical frequency," in *Proc. 22nd Int. Conf. Elect. Mach.*, 2016, pp. 1841–1846.

[18] M. Paradkar and J. Böcker, "Analysis of eddy current losses in the stator windings of IPM machines in electric and hybrid electric vehicle applications," in *Proc. 8th IET Int. Conf. Power Electron., Mach. Drives*, 2016, pp. 1–5.

[19] N. Bianchi and G. Berardi, "Analytical approach to design hairpin windings in high performance electric vehicle motors," in *Proc. IEEE Energy Convers. Congr. Expo.*, 2018, pp. 4398–4405.

[20] J. Chin, K. Cha, M. Park, S. Park, E. Lee, and M. Lim, "High efficiency PMSM with high slot fill factor coil for heavy-duty EV traction considering AC resistance," *IEEE Trans. Energy Conv.*, early access, Nov. 2, 2020, doi: 10.1109/TEC.2020.3035165.
[21] S. Park, E. Lee, J. Park, S. Hwang, and M. Lim, "Prediction of mechanical loss for high power density PMSM considering eddy current loss of PMs and conductors," *IEEE Trans. Magn.*, vol. 57, no. 2, Feb. 2021, Art. no. 6300205.
[22] E. Lee, S. Kwon, and J. Hong, "Thermal and electrical characteristics of EV traction motor considering AC resistance of MSO coil," in *Proc. IEEE Transp. Electrific. Conf. Expo.*, 2018, pp. 84–89.
[23] E. Lee, S. Kwon, H. Lee, S. Lee, and K. Lee, "Method for manufacturing MSO coil and device for manufacturing same," US Patent: 20200099279, 2020.
[24] J. Pyrhonen, T. Jokinen, and V. Hrabovcova, *Design of Rotating Electrical Machines*, 2nd ed. Hoboken, NJ, USA: Wiley, 2013.
[25] K. Diao, X. Sun, G. Lei, G. Bramerdorfer, Y. Guo, and J. Zhu, "System-level robust design optimization of a switched reluctance motor drive system considering multiple driving cycles," *IEEE Trans Energy Conv*, early access, Jul. 15, 2020, doi: 10.1109/TEC.2020.3009408.
[26] X. Sun, Z. Shi, G. Lei, Y. Guo, and J. Zhu, "Multi-objective design optimization of an IPMSM based on multilevel strategy," *IEEE Trans. Ind. Electron.*, vol. 68, no. 1, pp. 139–148, Jan. 2021.
[27] J. Chin, K. Cha, J. Park, D. Kim, J. Hong, and M. Lim, "Investigation of AC resistance on winding conductors in slot according to strands configuration," *IEEE Trans. Ind. Appl.*, vol. 57, no. 1, pp. 316–326, Jan./Feb. 2021.
[28] M. Lim, S. Chai, J. Yang, and J. Hong, "Design and verification of 150-krpm PMSM based on experiment results of prototype," *IEEE Trans. Ind. Electron.*, vol. 62, no. 12, pp. 7827–7836, Dec. 2015.
[29] D. Kim, J. Chin, J. Hong, and M. Lim, "Performance prediction of surface-mounted permanent magnet synchronous motor based on ring specimen test result," *IET Elect. Power Appl.*, vol. 13, no. 9, pp. 1280–1286, 2019.
[30] Y. Jung, M. Lim, M. Yoon, J. Jeong, and J. Hong, "Torque ripple reduction of IPMSM applying asymmetric rotor shape under certain load condition," *IEEE Trans. Energy Convers.*, vol. 33, no. 1, pp. 333–340, Mar. 2018.
[31] D. Kim, P. Benoliel, D. Kim, T. Lee, J. Park, and J. Hong, "Framework development of series hybrid powertrain design for heavy-duty vehicle considering driving conditions," *IEEE Trans. Veh. Technol.*, vol. 68, no. 7, pp. 6468–6480, Jul. 2019.
[32] T. Markel *et al.*, "ADVISOR: A systems analysis tool for advanced vehicle modeling," *J. Power Sources*, vol. 110, no. 2, pp. 255–266, 2002.
[33] K. Cha, D. Kim, Y. Jung, and M. Lim, "Wound field synchronous motor with hybrid circuit for neighborhood electric vehicle traction improving fuel economy," *Appl. Energy*, vol. 263, 2020, Art. no. 114618.

Kyoung-Soo Cha received the bachelor's degree in electrical engineering from Chungbuk University, Cheongju, South Korea, in 2015. He is currently working toward the Ph.D. degree in automotive engineering with Hanyang University, Seoul, South Korea.

His research interests include electric machine design for automotive, home appliance, rare-earth free machine, and system-based design.

Jun-Woo Chin received the bachelor's degree in mechanical engineering, in 2014, from Hanyang University, Seoul, South Korea, where he is currently working toward the Ph.D. degree in automotive engineering.

His research interests include the design, losses and multiphysics analysis of electric machines for mechatronics systems such as automotive application.

Soo-Hwan Park received the bachelor's degree in mechanical engineering, in 2014, from Hanyang University, Seoul, South Korea, where he is currently working toward the Ph.D. degree in automotive engineering.

From 2019 to 2020, he was with the Korea Institute of Industrial Technology, South Korea. His main research interests include electromagnetic field analysis, design and optimization of electric machines for automotive and robotics applications, and electric machine drive for industrial applications.

Young-Hoon Jung received the bachelor's degree in mechanical engineering in 2013 and the integrated master's and Ph.D. degrees in automotive engineering from Hanyang University, Seoul, South Korea, in 2020.

Since 2020, he has been with the R&D Division of Hyundai Motor Company, Hwaseong, South Korea, where he is currently a Senior Research Engineer. His research interests include electric machine design for automotive and robot applications, and ultra-high speed motors.

Eui-Chun Lee received the bachelor's degree from Kumoh National Institue of Technology, Gumi, South Korea, in 2014, and the master's degree from Kyung-Pook National University, Daegu, South Korea, in 2016, both in mechanical engineering. He is currently working toward the Ph.D degree in automotive engineering from Hanyang University, Seoul, South Korea.

Since 2019, he has been with the Korea Institue of Industrial Technology, where he is currently a Researcher at Safety System R&D Group. His main research interests include HEV, EV, robot, drone drive motor design and productive electric machine manufacturing process.

Myung-Seop Lim (Member, IEEE) received the bachelor's degree in mechanical engineering and the master's and Ph.D. degrees in automotive engineering from Hanyang University, Seoul, South Korea, in 2012, 2014, and 2017, respectively.

From 2017 to 2018, he was a Research Engineer in Hyundai Mobis, Yongin, South Korea. From 2018 to 2019, he was an Assistance Professor with Yeungnam University, Daegu, South Korea. Since 2019, he has been with Hanyang University, Seoul, South Korea, where he is currently an Assistant Professor. His research interests include electromagnetic field analysis and multiphysics analysis of electric machinery for mechatronics systems such as automotive and robot applications.